



OPEN

The physico-chemical and antimicrobial properties of nano ZnO functionalised tannic acid

Nurul Akmal Che Lah^{1,2✉} & Aqilah Kamaruzaman^{2,3}

Tannic acid (TA) has been reported as an efficient plant-based compound with inhibitory activity against viruses and bacteria. The combination of TA with Zinc Oxide (ZnO) nanostructures with ZnO is one of the most widely used nanoparticles for antimicrobial properties, have not yet fully elucidate especially their mechanisms of overall physicochemical and antimicrobial actions. Hence, to observe the influence of TA adsorption on ZnO, the investigations on the TA concentration and the effect of pH towards the physicochemical, optical and antimicrobial properties are demonstrated. The pure ZnO are synthesised via the chemical reduction method and the ZnO-TA nanostructures are further prepared using the dropwise methods to form variations of pH samples, which causes the formation of different mean particle size distribution, d_m . The findings reveal that the performance of physicochemical and optical properties of pure ZnO and ZnO-TA are different due to the wrapped layers of TA which change the charged surface of all the particles. The protonation reactions yield strong pH dependence (pH 3 and 5), with uptake performance becoming more dominant at higher TA concentration loading (pH 3). The detailed optical energy bandgap and Urbach energy that concluded the nanoparticle growth and disorder condition of produced particles are presented. For antimicrobial efficiency, ZnO-TA shows improved effectiveness in growth inhibitions of *S. aureus* 99.69% compared to pure ZnO nanostructure (99.39%). This work reveals that the TA concentration increases the overall performance, and the discussion gives added support to their potential performance related to the field of ZnO compound.

Keywords Zinc oxide, Tannic acid, Optical bandgap, Urbach energy, Physicochemical properties, Antibacterial action

Recently, one of the most widely studied natural plant constituents for good inhibitory activities against severe acute respiratory syndrome coronavirus 2 (SARS-CoV-2) activated by the activating protease¹⁻⁴ and the transmembrane protease serine 2 (TMPRSS2)³⁻⁷ for a broad range of respiratory viruses is the functionalised tannic acid (TA). Not only applicable to viruses but a range of bacteria also, including *Pseudomonas aeruginosa* (*P. aeruginosa*)⁸⁻¹⁰ and *Staphylococcus aureus* (*S. aureus*)¹⁰⁻¹², the global primary factor of human infectious diseases by affecting their enzymatic activities in the presence of phenolic hydroxyl groups of TA. In this respect, the phenolic compounds play a crucial role in determining the effectiveness of the antimicrobial activity, which is believed to be conquered by the mechanism action, such as reduced bacterial metabolism and induction of efflux pumps¹³⁻¹⁶. The tannins of TA disrupt the cell wall of microorganism by passing through the internal membrane and interfere the metabolism reaction of the cell. Parallely, an efflux pump is an advanced defence system against antimicrobials and tannin reduces the induction of the efflux pump and indirectly increases the concentration of drugs inside the microorganisms. In essence, TA is the most important representative of the hydrolysable tannins family. It consists of a monosaccharide core, often known as glucose, in the centre and is a weak acid. TA derivatives establish high occupancy in metal-organic coordination complex bonds with transition metal ions forming heterogeneous bionanostructures in the direction of green chemistry¹⁷⁻²¹. In the view of green chemistry, the employment of TA is able to enhance biocompatibility and the features of metal-TA

¹Centre for Advanced Intelligent Materials, Universiti Malaysia Pahang Al-Sultan Abdullah, Lebuhraya Tun Khalil Yaakob, 26300 Gambang, Pahang, Malaysia. ²Faculty of Manufacturing and Mechatronics Engineering Technology, Universiti Malaysia Pahang Al-Sultan Abdullah, 26600 Pekan, Pahang, Malaysia. ³City Universiti Malaysia, 8, Jalan 51a/223, Seksyen 51a, 46100 Petaling Jaya, Selangor, Malaysia. ✉email: akmalcl@umpsa.edu.my

complexes can yield metal-mediated self-assembly with good physicochemical and other properties capability. Among them, ZnO-TA is one of the emerging molecular nanostructures of metal-polyphenol, mostly used in therapeutics (both therapy and diagnosis) applications due to the excellent integration of imaging moieties and therapeutic agents in one package.

ZnO proves to be one of the appealing antibacterial nano agents that have been heavily researched against a wide range of bacterial species^{22–25}. As noted for other nanometals, their increase in specific areas increases particle surface activity, leading to excellent interaction with the surface and/or the core of the bacteria, which gives specific bactericidal mechanisms to inhibit bacterial growth. So as ZnO nanostructures, their potent antimicrobial properties against a multitude of microorganisms, antidiabetic and acaricidal activities depend on their concentration, size, morphology and stability^{26–28}. The surface modification of ZnO with TA could be one of the remarkable means that have not yet been widely implemented as newly generated bioactive nanostructures^{29–33}. On the antibacterial properties of these newly surface-modified nanostructures, there is scarce information available compared to existing publications on physicochemical properties. Hence, it is important to understand the intrinsic interaction between the ZnO and TA to improve its overall effectiveness and efficiency and make it regarded as a good contender in biocompatible applications.

To optimise the medium reaction condition and growth efficiency, appropriate molar concentration is essential to ensure the achieved aim. It shall be noted that TA typically belongs to the large natural polyphenol^{34–36}, which can easily bind to the various metal ions to form highly stable metal complexes via the produced polydentate ligands. Therefore, unlike a small polyphenol molecule, a large one can induce the self-assembly of ZnO-TA^{34,37–39}. However, it can also cause the ZnO nanostructures to be submerged entirely into the island phenotypes. The ideal concentration of chemical variants that yield specific moieties of pH is important to observe how chemical modification changes the activity level and further affects the overall properties of the as-produced ZnO-TA nanostructures.

Herein, the present study investigated the effect of different molar concentrations of hydrolysable TA for their ability to produce different particle sizes/morphologies of ZnO nanostructures and further modified the overall physicochemical properties based on the changes in pH. Understanding the effect of structural features from the consequences of finetuning of derivatisation at the molecular interaction permits hints related to the incorporation of tannin functionalisation with respect to the synthesised ZnO nanostructures. Therefore, the work endeavours to report the evidence of physicochemical and antimicrobial characteristics for TA-induced ZnO nanostructures. Also, the highlight of the overall changes in pH value due to the changes in particle size distribution is assessed further in terms of intrinsic optical Urbach energy and optical bandgap. The findings of the work fill the scarcity of structure–activity relationships and interaction mechanisms in the field of bionanocatalyst phenolic compounds.

Material and method

Materials

ZnO-TA nanostructures were prepared using the simple hydrothermal method with an additional sodium citrate (SC) as the surface modification agent in an aqueous solution. Zinc acetate dehydrates $\text{Zn}(\text{CH}_3\text{COO})_2 \cdot 2\text{H}_2\text{O}$ (>99%, Merck, UK) is used as a precursor, tannic acid, TA ($\text{C}_76\text{H}_{52}\text{O}_{46}$) powder (R&M Chemical, Malaysia) as surface modification and trisodium citrate simply known as sodium citrate, SC ($\text{Na}_3\text{C}_6\text{H}_5\text{O}_7 \cdot 2\text{H}_2\text{O}$, >99%, R&M Chemical, Malaysia) as a refining agent. Distilled water (Material Laboratory Faculty of Manufacturing and Mechatronics Engineering Technology, Universiti Malaysia Pahang Al-Sultan Abdullah) is a solvent. All chemicals used were of analytical grade and without further purification.

Preparation of ZnO nanostructures

0.05 M zinc acetate dehydrate is vigorously mixed and added dropwise with 0.008 M SC with slow stirring for 20 min at 70 °C to obtain a homogenous mixture. The formation of white suspension is observed and continuously stirred for 5 h. Stock standard solutions of each chemical reactant are produced straightly by weighing and diluting with ~90% water to a known volume. The white-coloured sediment formed is centrifuged (1000 rpm for 10 min) and rinsed a few times with distilled water. The aim is to wash off those impurities that caused improper low stability.

Preparation of ZnO-TA nanostructures

For the effect of TA solution on the synthesised ZnO nanostructures, each concentrated sample is diluted with 50 ml of distilled water and added dropwise with TA to check the influence of TA on the aggregation formation of ZnO nanostructures. For this purpose, the effects of with and without TA in the as-synthesised ZnO nanostructures sample are monitored compared to initial concentration reactant samples. The added concentrations of TA are 50 and 300 μl . The concentration of TA is calculated based on the equation⁴⁰:

$$c = \frac{m}{v} \times \frac{1}{MW} \quad (1)$$

where c refers to molar concentration (mol l^{-1}), m is the solute mass (gram), v is the solution volume (L), and MW is the molecular weight of the element (g mol^{-1}). The pH measurement for each sample is taken after each dropwise process.

pH measurement

The as-synthesised ZnO-TA samples were diluted for 50 and 300 μM of TA, and a pure ZnO sample was used for all spectroscopic measurements. The pH was measured using the pH strip (Natural Care, Park City, UT). The pHs before and after the dilution are shown in Table 1.

Morphological measurement

The morphological and particle size distribution analyses of the samples were carried out via transmission electron microscope (TEM, 3000F, JEOL, Japan) run at 300 kV. Samples for TEM were prepared by dropping the suspension of the ZnO nanostructure onto a lacey carbon copper-coated grid specimen holder and dried under ambient conditions for 24 h. The TEM micrographs were obtained at different magnifications and further examined using Gatan Micrograph software. Meanwhile, the surface morphology of the samples was observed using field-emission scanning electron microscopy (FESEM, JEOL JSM-7800F, JEOL, Japan) equipped with dispersive energy X-ray (EDX LSM880-FESEM, Carl Zeiss AG, Germany) with magnification of $\times 125,000$ and $\times 20,000$ at an accelerating voltage of 5 kV. For FESEM-EDX, the solutions were dropped onto the aluminium foil substrate and left to dry for 24 h prior to the observation.

Optical measurement

The optical absorption spectra evaluation was done using a UV-Vis spectrophotometer (Shimadzu-UV-1800 UV-Vis Spectrophotometer, Japan) in the wavelength range of 200 to 800 nm at the rate of 200 nm/min. The solution sample was diluted based on the nanosolution to a solvent dilution ratio of 1:6. The 4.0 ml diluted suspension was then pipetted into the quartz cell for the test. Prior to the test, a baseline measurement was conducted to measure a 0% correction for each wavelength in the scan to ensure accurate absorbance measurement. The range of absorbance spectra is between 200 and 800 nm. The obtained spectra are further used to plot the Tauc plot to determine the energy band gap of the sample. The variation in the optical band gap is based on the Tauc relation using the relation of^{41,42}:

$$(\alpha h\nu)^2 = A(h\nu - E_g)^n \quad (2)$$

where n is $\frac{1}{2}$ for direct band gap materials and 2 for indirect band gap materials. The dependency of interband transition is on A , the absorbance, the photon energy is referred by $h\nu$ and the optical band gap is designated by E_g .

In general, the absorption coefficient, α is often displays an exponential tail below the optical bands. These so-called Urbach tails, E_U is defined using the following equation^{43,44}:

$$\alpha = \alpha_0 \exp\left(\frac{E}{E_U}\right) \quad (3)$$

with the α referring to the spectral dependence of absorbance coefficient, α_0 is the constant, E is known as $h\nu$ that represents the photonic energy (eV) and E_U is the Urbach energy quantifying the total energetic disorder of the system. The reciprocal slope of the linear fitting from the plot of $\ln \alpha$ (cm^{-1}) versus photon energy (eV) gives the E_U based on the following equation⁴⁵:

$$E_U = \frac{1}{\text{slope}} \quad (4)$$

Besides, the emission properties were carried out using photoluminescence spectroscopy (Edinburgh Instruments- NIR 300/2, UK) to analyse the prepared sample's emission spectrum. All the PL measurements were set at an excitation wavelength of 900 nm using 325 laser excitations by a Xenon lamp with a 1.1 mm diameter optical aperture under the same optical conditions at room temperature. The incident laser power was varied using filters with different optical densities. The similar prepared solution, as mentioned for UV-Vis sample preparation, is used for PL measurement.

Chemical measurement

In evaluating the chemical bonding structure of the sample, the attenuated total reflectance (ATR) Fourier transform infrared (FT-IR) Spectrometer (Perkin Elmer-Spectrum 100, USA) was run in the wavenumber region of 4000–400 cm^{-1} with 32 scans at a resolution of 2 cm^{-1} . FTIR is employed to identify the unknown organic components in as-produced ZnO and ZnO-TA samples to determine the purity of elements/samples. The solution

Temperature ($^{\circ}\text{C}$)	Zn precursor (g)	SC (g)	TA (μL)	Concentration of TA (M)	pH
70	0.4	0.2	0	0	7
			50	0.21	5
			300	1.24	3

Table 1. Parameters used in preparing pure ZnO and ZnO-TA via hydrothermal method. The concentration of TA varies to obtain different pH values.

samples were dropped onto the thick glass substrate positioned at the sample holder of the ATR-FTIR spectrophotometer. The transmittance of the solution was then measured.

Structural measurement

The crystal phase composition and crystallinity of the sample were examined using X-ray diffractometry (XRD, Bruker AXSD8 Advance, Germany) with a Cu K α radiation source ($\lambda = 1.5405 \text{ \AA}$) operating at 45 kV and 100 mA. The spectra were measured in the range of 5–80° with a step size of 0.026°. The powdered sample was prepared using the drop method. The solutions of the suspension sample are dropped on the thin glass substrate and left to dry in a vacuum cabinet for 12 h. For the crystallite size, Debye–Scherrer's equation is used to determine the crystalline size structure, D based on the plot of diffraction and relation to Bragg's Law^{46,47}:

$$D = \frac{k\lambda}{\beta \cos\theta} \quad (5)$$

where K is referring the dimensionless shape factor with a value close to unity (0.9), λ is the X-ray wavelength while β refers to the line broadening at half the maximum intensity (FWHM) and θ refers to the Bragg angle in degree unit. Meanwhile, the crystallinity percentage of the sample is calculated from the area of XRD peaks using the relationship of⁴⁸:

$$\text{Crystallinity} = \frac{\text{Area of crystalline peak}}{\text{Area of all peaks (crystalline + amorphous)}} \times 100 \quad (6)$$

Antimicrobial susceptibility measurement

The AATCC-100 method is applied to determine the minimum inhibitory concentration (MIC) to evaluate the pure ZnO and ZnO-TA nanostructures's antimicrobial sensitivity in vitro. The test used the drug-resistant human pathogen *S. aureus* (ATCC 25,923). After a pure culture is isolated, MICs are determined using broth dilution methods (in liquid growth media). The bacterial reduction percentage is calculated based on the efficacy calculation⁴⁹:

$$\text{Bacterial reduction efficiency from challenge inoculums \%} = \frac{A - B}{A} \times 100\% \quad (7)$$

where A is the number of bacteria recovered from the inoculated treated test specimen immediately after inoculation (CFU/sample) and B is the number of bacteria recovered from the inoculated treated test specimen over the contact period (CFU/sample).

Result and discussion

Morphological analysis

The morphological properties of the as-synthesised pure ZnO and ZnO-TA nanostructures are analysed based on the micrograph of TEM and FESEM. As depicted in Fig. 1, it is clear that the TEM micrograph of pure ZnO and ZnO-TA shows distinctive dispersion conditions from each other due to the addition effect of TA. As presented in the images, all samples were primarily spherical in shape and dispersed within the island of tiny clusters of various sizes. For pure ZnO nanostructures (Fig. 1a), the mean particle diameter, d_m are smaller compared to the ZnO-TA samples (Fig. 1b,c) with the $d_m \sim 8 \pm 0.5$, 18 ± 0.4 and 23 ± 1 nm, respectively.

The role of pH is significant where the pH value decreases when adding TA is increased. The pH is the fundamental indicator for materials' properties and to determine the net charge of TA function on the samples. pH of pure ZnO (pH ~ 7) is considered the neutral pH and initial pH of the sample with zero added TA. In this case, pH 5 (50 μL) is regarded as the stable pH value where most of the particles are individually separated with better narrow Gaussian size distribution and cumulative percentage distribution. Meanwhile, a higher concentration (300 μL) of TA reached the pH of 3, leading to larger d_m of nanostructures and the formation of connected flat haze particles surrounding the structures. These conditions proved that the aggregation and accumulation have occurred as the TA creates an acidic environment. The condition is due to the releasement of free electrons in the form of an oxygen ring, which then reacts with the phenolic groups of TA. As more phenols are introduced, a higher amount of protonation of active sites on positively charged Zn is created and alters the phenol adsorption, which yields more aggregation nanostructure of the system.

As the TA are added, aggregation is induced, resulting from the coalescence of small particles from the attachment growth that depends wholly on the volume of the projected particles of the samples. The merging of the particles is helped by the minor fluctuations caused by the acidic surroundings, which created a jump to contact. This condition is known as oriented attachment (OA) or oriented aggregations, a crucial crystal growth mechanism^{50,51}. This can be considered direct evidence of OA, which reveals the necessary changes in the structure and surface chemistry of the nanocrystals, the solvent between the crystal and the resulting particles' response to the surroundings. In acidic conditions, proton attack at the surface of ZnO is high^{52,53}. Generally, at lower pH (pH 5 and 3), the tendency to produce a soluble Zn²⁺ and Zn(OH)⁺ ion is higher. Therefore, the aggregation occurred as the phenolic group's protonation took place, which reduced the functional group's reachability to squeeze between the ZnO nanocrystals (jump contact) and created a larger attached particle. Upon contact, the connecting neck between the particles has vanished. Apart from this, the drying process for TEM sample preparation also promotes non-homogeneous deposition. Thus, the aggregation of ZnO nanostructures is inevitable as the solvent evaporates.

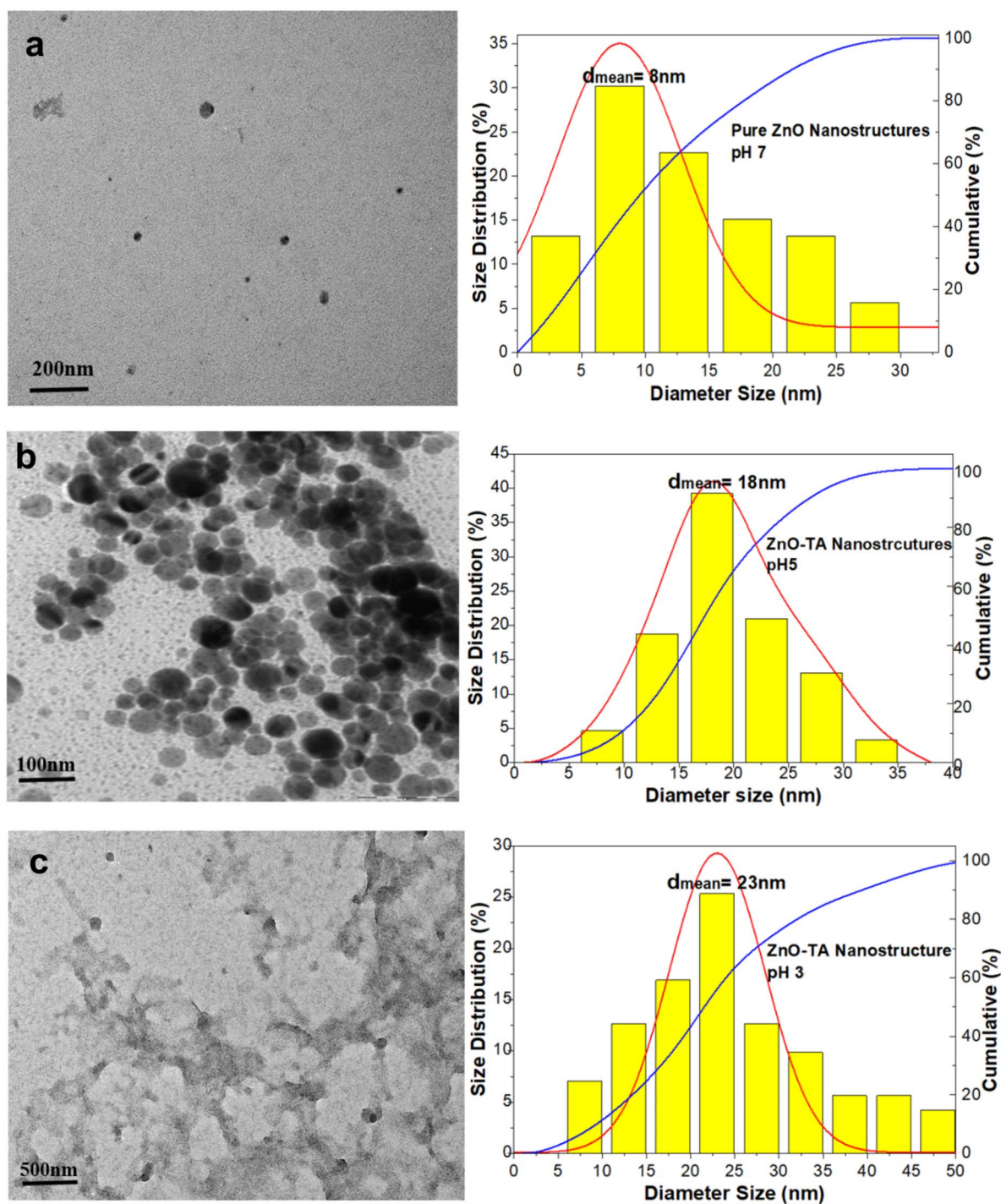


Figure 1. TEM micrograph of synthesised (a) pure ZnO (pH 7), (b) ZnO-TA at pH 5 and (c) pH 3 nanostructures with the $d_m \sim 8 \pm 0.5$, 18 ± 0.4 and 23 ± 1 nm, respectively. The Gaussian (red line) and cumulative percentage (blue line) fittings for each sample are also included.

The micrographs of FESEM reveal the morphological characteristics of both pure ZnO and ZnO-TA nanostructures, as depicted in Fig. 2. The pure ZnO nanostructures were shown to dominantly have cube-shaped structures that appeared to be aggregating together, causing agglomeration with different forms of irregular shape clusters, as indicated in Fig. 2a. It is noted that the aggregation of nanostructures is clearly visible for all samples and mainly formed during the drying process of the FESEM samples. Similar morphology and aggregation conditions were observed from a few reported works on ZnO nanostructures. The associated EDX of FESEM indicated the presence of Zn and O as significant elements with a mass of 77.33% and 19.92%, respectively. The results proved that the synthesised pure ZnO nanostructures are of high purity, representing high Zn and O element compositions. Note that the small mass per cent of Al element (0.275%) is due to the aluminium foil used as a substrate for FESEM viewing. Interestingly, there is no trace of SC from the mass per cent, proving that the

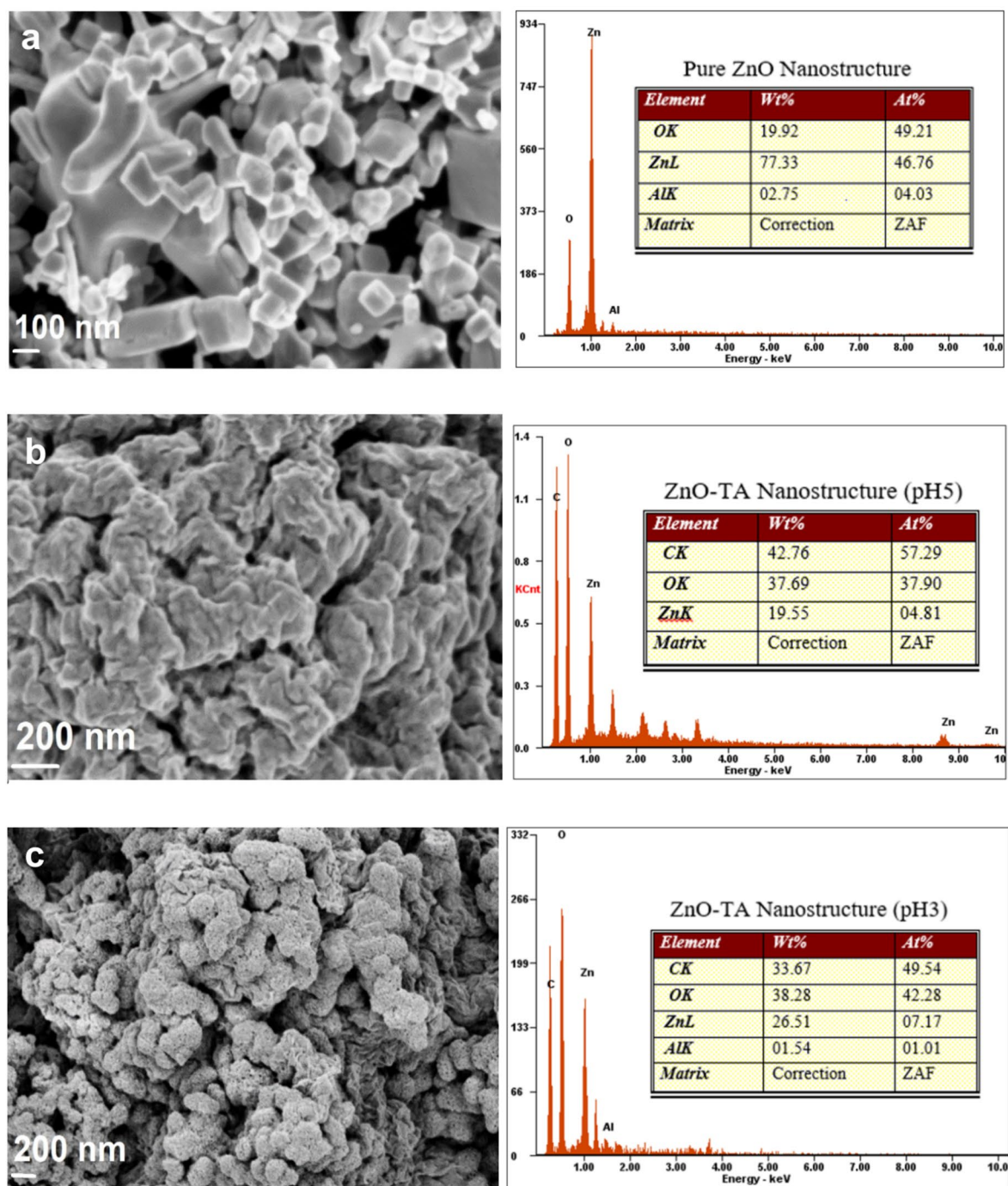


Figure 2. FESEM microscopic image with corresponding EDX graph on (a) pure ZnO, ZnO-TA at (b) pH 5 and (c) pH 3 nanostructures. The small percentages of Al and Mg compositions are due to the use of aluminium foil as a substrate during viewing.

emulsifying agent is entirely removed during centrifugation. As a comparison, the attained morphologies and size variations of ZnO-TA nanostructures at pH 5 and 3 are shown in Fig. 2b,c, respectively. The aggregation of nanostructures is significant and the initial morphology of cuboids changed into irregular bounded grain clusters with no specific geometry upon the influence of pH from the addition of TA. As mentioned beforehand, the nanostructures appeared to be bound together into a continuous aggregation of various sizes with a decrease in pH attributed to the increase of ionisation of TA. At low pH conditions ($\text{pH} < 6$), ionisation of TA is weak, as described by the equation:



Chemical bonding description

ATR-FTIR is one of the confirmatory techniques for chemical functional group and demonstrates the bonding behaviour, such as the vibrational and rotational modes of the existing molecules, which help to identify the functional and possible phytochemical molecules involved in the stabilisation of pure ZnO and ZnO-TA nanostructures, as depicted in Fig. 3. For pure ZnO nanostructures (denoted as pH 7), the presence of broad peak at the region around 2069 cm^{-1} indicated the O–H stretching and deformation in the external band of pure ZnO nanostructures caused by the water adsorption on the surface of Zn⁵⁴. A small hump in the range of $1385\text{--}1637\text{ cm}^{-1}$ demonstrated the presence of an O–C–O band and C=O stretching⁵⁵. Both types of stretching of O–C–O and C=O are due to the atmospheric absorption at the preparation time of the sample in the non-vacuum system. Additionally, several small humps have been formed around $708\text{--}1096\text{ cm}^{-1}$, proving the presence of C–H and =C–H functional groups⁵⁶. The effect of SC causes the minimal amount of carbon-hydrogen active group. Meanwhile, the presence of the peaks of 533 cm^{-1} is due to the stretching mode of ZnO⁵⁷.

In comparison, the presence of adsorbed TA molecules as functional groups on the surface of ZnO nanostructures are also provided. TA has yielded some chemical alterations on the surface of pure ZnO nanostructures during the formation process. As for ZnO-TA samples (pH 5 and pH 3), the sample showing combines region peaks as pure ZnO nanostructure and TA. A broadband of pure TA at 3467 cm^{-1} , has altered the position of the intense peak in pure ZnO nanostructures⁵⁸, which is believed to have originated from the presence of polyphenols of TA. This band is assigned to the broad hydroxyl groups (O–H)-stretching bonded and strong of C–H (aromatic medium), causing the shifting to 2063 cm^{-1} (pH 5) and 3447 cm^{-1} (pH 7) upon the addition of TA⁵⁹. TA also shows a slight hump at the peak of 2056 cm^{-1} which is due to the C–H stretching vibration of alkane groups with some aromatic esters due to the signal characteristics of carbonyl groups C=O stretching (1539 cm^{-1}) and C–O (1349 cm^{-1})⁶⁰. Besides, the significant difference between pure ZnO and ZnO-TA nanostructures is the increasing peak presence in the region between 700 and 1500 cm^{-1} . This region indicates the stretching of the C=O and C–O bonds. The peak around this region is insignificant for pure ZnO at pH 7 as the carbon elements only present C–O due to non-vacuum conditions during synthesising. Meanwhile, the stretching is dominant for ZnO-TA due to the presence of element C=O in TA. A similar behaviour is reported in the recent literature that observed the bonding reaction between ZnO, TA and the waste bagasse sample⁶¹. As we know, TA molecules are $\text{C}_7\text{H}_5\text{O}_4$. Thus, the increase of carboxylate element dominates in the associated samples⁶². The spectral signatures of carboxylate impurities essentially increase, indicating the possible association of phenolic group form TA with zinc carboxylate and conversion to ZnO during synthesis. The intensity of the hydroxyl peak follows an increasing trend in ZnO-TA samples compared with the synthesised pure ZnO nanostructure sample. The peak at the 577 and 593 cm^{-1} region shows the Zn–O bonding in both pH5 and pH3, respectively. The peaks are slightly shifted compared to pure ZnO nanostructure samples. The shift may be associated with oxygen deficiency and oxygen vacancy defect complex in the ZnO nanostructures⁶³. The intensity of the oxygen-deficiency-related defect-complex band does not appear to change much on the particle size, but it indicates the probability of bulk defects.

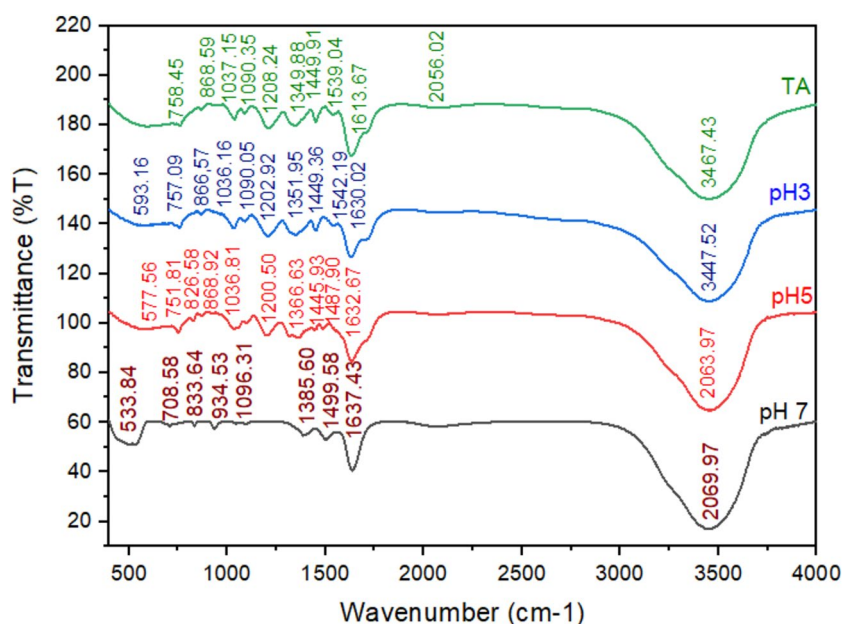


Figure 3. Chemical bonding studies from ATR-FTIR indicate the bonding types available in pure ZnO (pH 7) and ZnO-TA nanostructure (pH 3 and pH 5). The effect of functional groups present in TA structure is also evaluated for comparison.

Brønsted-Lowry acid–base relation

The conditions of ZnO-TA nanostructures are further discussed based on the Brønsted-Lowry acid–base interactions. The Lewis hard and soft acids based on Brønsted-Lowry acid–base theory is commonly used in explaining the intrinsic interaction involving metal–ligand inorganic chemistry for the stability of nanostructures and their compounds. The information also provides an understanding of the related reaction mechanisms yielding the morphological transition phenomenon. In this case, as the TA is introduced to the ZnO nanostructures, the phenolic hydroxyl groups of TA adsorbed on the surface of ZnO, yielding a Brønsted base surrounding the highly acidic medium. The tendency to accept the protons created from the reaction is high.

This also can explain the increase in d_m condition of the ZnO-TA nanostructures and the change in morphological structure upon introducing TA to the pure ZnO due to the changes in the pH medium (from neutral to acidic medium). TA is an acidic solution that has a high concentration of phenolic hydroxyl ions. This proved the increase of OH⁻ ion density in the sample that gives effects on the morphological changes according to the net results of dynamic growth explained by the Ostwald ripening (OR) phenomenon⁶⁴. In this case, the classical crystal model of OR occurs as soon as the particles of ZnO react with an acidic solution, inducing small crystalline nuclei aggregation. As mentioned previously regarding the oriented attachment mechanism, this mode is a process that took OR as part of the reaction in which the dissolution, precipitation, and ripening during the particle motion, collision, and aggregation processes formed those unique crystallographic orientations of ZnO-TA. Hence, the difference is that the formation of complex nanostructure crystals with wide varieties of morphologies, including the irregular nano geometry, is mainly explained by oriented attachment, which cannot be justified by classical OR⁶⁵.

As mentioned beforehand, the morphological transition of the samples are due to the change of the pH. Hence, the pH changes are determined based on their surface conditions of acidity or basicity. Employing the concept of Lewis hard and soft acid bases, the stability condition of pure ZnO and their compound, ZnO-TA, including the associated reaction mechanisms and the prediction of reactivity of frontier molecular orbital (FMO) theory observing the interaction of Highest Occupied Molecular Orbital (HOMO)-Lowest Unoccupied Molecular Orbital (LUMO) activity can be deduced⁶⁶. ZnO nanostructures is considered as an hydroxylated due to the interaction of the atmospheric water vapour and oxygen, O₂, to a certain level under typical atmospheric conditions. Herein, the TA that consists of those phenolic hydroxyl acts as Brønsted base spots, which enable the acceptance of protons from the Zn ions (Zn²⁺) from the exciton dissociation mechanism stimulated by the charge transfer. Notably, the cationic Zn²⁺ centres acts as Lewis acidity site by accepting electron pair and giving the LUMO energy whilst the spin excitation of oxygen ion (O₂⁻) acts as Lewis bases creates energy barrier for HOMO⁶⁷. In this case, the interaction of Zn²⁺ (LUMO) coordinated with the hydroxyl TA ligand (HOMO) formed atomic bonding orbitals known for intimate orbital (HOMO–LUMO) interaction yielding the description of produced properties. High frontier orbital gap of HOMO–LUMO gives high kinetic stability which cause the reduce the chemical reactivity. Hence, the chemical reactivity bestows for the rate of morphological changes for different pH (mild acidic 3 > pH < 7) of ZnO-TA nanostructures.

Optical analysis

Absorption description

The absorbance spectra of the as-synthesised pure ZnO and ZnO-TA with the corresponding TA spectrum are presented in Fig. 4. The significant difference can be seen for pure ZnO at pH7, where the observed absorbance peak with low intensity is found at 298 nm wavelength. For ZnO-TA with pH 5 and 3, the exhibited peaks are at 308 and 313 nm, shifting towards longer wavelengths as the pH values decrease due to the increases in TA concentration. This is in line with the proof of morphologies of TEM and FESEM that have been discussed beforehand. As shown in the spectra, TA has a peak at 330 nm, and this indicates that the TA layer in ZnO-TA nanostructures has imparted noticeable changes in the absorbance of pure ZnO. One is assuredly the oxygen-rich ZnO phase, whose absorption band is in the vicinity of that of the original pure ZnO phase. Theoretically, the TA tends to slowly dominate the ZnO nanostructure and causes an increase in the number of free electrons. This caused an increase in the acidity of the ZnO samples, which then affected the structure (tend to disaggregate the structures) and increased the reactivity of the nanoparticle. The reactivity of phenolic hydroxyl groups contributed from the TA structure increased the amount of oxygen anions⁶⁸ which then imparted in the reaction with ZnO ions to establish a stable five-numbered ring complex. The condition encouraged the relocation of the lone pairs associated with the other two hydroxyl groups and stabilised the complex.

The second factor is the chemical inhomogeneity due to the presence of a higher amount of oxygen with the existence of a phenolic group of TA³⁴. In addition to the band shift, the absorption band becomes distinctly narrow with increasing oxygen elements. The narrow band in ZnO-TA is assigned to the overlap of multiple spectral phases with distinctive chemical bonding states and stoichiometry system (inhomogeneous broadening), as verified by the FTIR results in the previous section. Inhomogeneity appears naturally from the dissimilarity in the number of valence electrons between oxygen and the extension of H-bonding atoms. That is to say that pure ZnO and ZnO-TA are promoted by their own microscopic crystal structures, with the absence of crystal structure for ZnO-TA, thereby yielding ZnO-TA complexes.

Optical band gap

The changes in the optical bandgap structure with d_m variation between the pHs were studied using the conventional optical absorption technique, which involves measuring the optical absorption coefficient with the Tauc method. This typical method conclusively distinguishes between the different optical bandgaps corresponding to the extrapolation of the linear region of the Tauc plot, as indicated in Fig. 5 for both pure and ZnO-TA nanostructures.

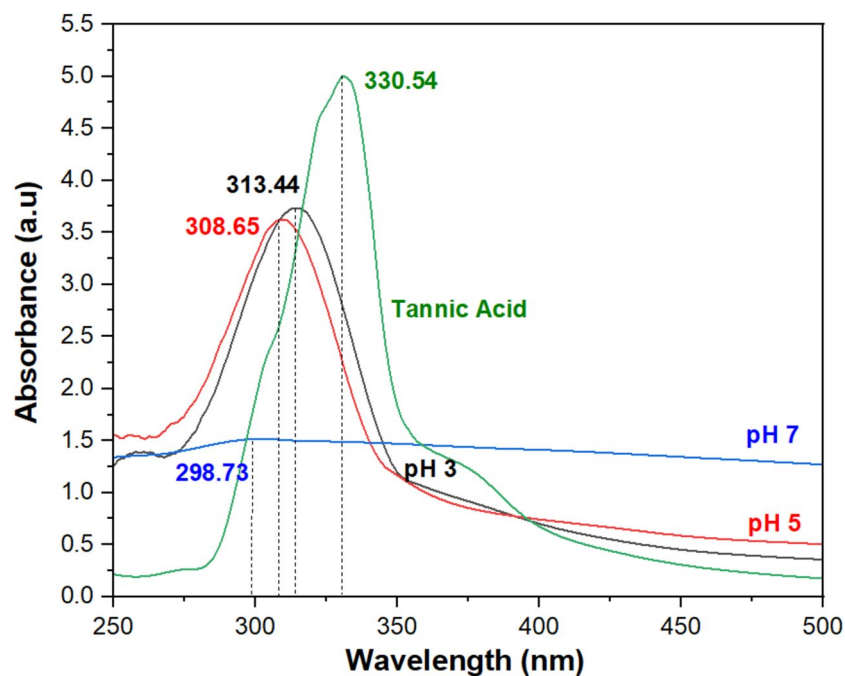


Figure 4. Absorbance spectra for both the pure ZnO and ZnO-TA at pH 7, 5 and 3. The absorbance properties of TA are also included for comparison.

Figure 5a shows the Tauc plot of the direct energy bandgap, E_g of pure ZnO nanostructure samples synthesised with the obtained optical E_g values of 3.45 eV. This indicated that the synthesised ZnO has E_g relevant to the values range reported by other works on pristine ZnO nanostructures. Conventional semiconductors have E_g between 1 and 1.5 eV, whereas wide-bandgap materials such as ZnO nanostructures have E_g between 2 to 4 eV. The corresponding experimental Tauc plot for ZnO-TA samples at pH 5 and pH 3 are shown in Fig. 5b,c. As TA concentration increases within the ZnO nanostructure system (decrease in pH), the shifting position of the UV absorption band to a shorter wavelength infers increasing E_g values to 3.56 and 3.59 eV for ZnO-TA at pH5 and pH3, respectively. As noted beforehand, as the higher concentration of TA is induced, the d_m of the prepared ZnO-TA nanostructures increases. As the size of ZnO nanostructures increases, fewer donor atoms of Zn are available, which provides fewer carriers that yield the shifting of Fermi level towards the conduction band and causes the widening of E_g . Particularly, the E_g widening is explained by the interaction of the unshared electrons of oxygen in the isolated phenyl group of TA with the p -electron sextet of the aromatic ring⁶⁹. The p band of phenols located entirely overlapping with the oxygen $2p$ band becomes non-occupied. Therefore, it is masked by a much more absorbing conjugated system and accordingly gives rise to an overlapping complex band system, which causes the valence band maximum to increase. Besides, the Zn $4s$ conduction band, which determines the minimum, is not affected by the addition of phenolic of TA. Nonetheless, due to the fusion effect of the valence band maximum shifting and the minimum conduction band, the E_g becomes wider compared to the pure ZnO nanostructure sample.

In fact, the application of a wider bandgap offers better merit for high-performance UV photodetector. This is also a core for the TA implication on ZnO nanostructures in terms of UV protection agents. It is noted that the calculations for both direct $(\alpha h\nu)^2$ and indirect $(\alpha h\nu)^{1/2} E_g$ of TA are compared and shown in Fig. 5d,e, respectively. TA is an amorphous semiconductor as the values (3.50 eV for $(\alpha h\nu)^2$ and 3.501 for $(\alpha h\nu)^{1/2}$) are similar to those of each semiconductor alone. Specifically, the typical amorphous semiconductor behaviour would be able to dominate the optical transition to a first approximation, which causes a significant charge localisation that leads to a substantial difference between the size of E_g .

Urbach energy

As depicted in Fig. 6, the absorption coefficient, α in both the pure ZnO and ZnO-TA nanostructures were extracted from the absorption results in Fig. 5. The inverse slope, m obtained from the linear approximation of the α as a function of photon energy gives the value of Urbach energy, E_U of the samples. A sharper onset of absorption represents the lower of E_U which implies an inverse value of E_g . The E_U is higher for pure ZnO with the value of 9.39 eV and further decreases at pH 5 giving the E_U of 1.99 eV. The lowest obtained E_U is at pH 3 with 0.78 eV. The E_U indicates the disorder phonon states decreases with increasing the amount of TA concentration (pH decreases) and causes the E_g to increase, which has been summarized in Table 2.

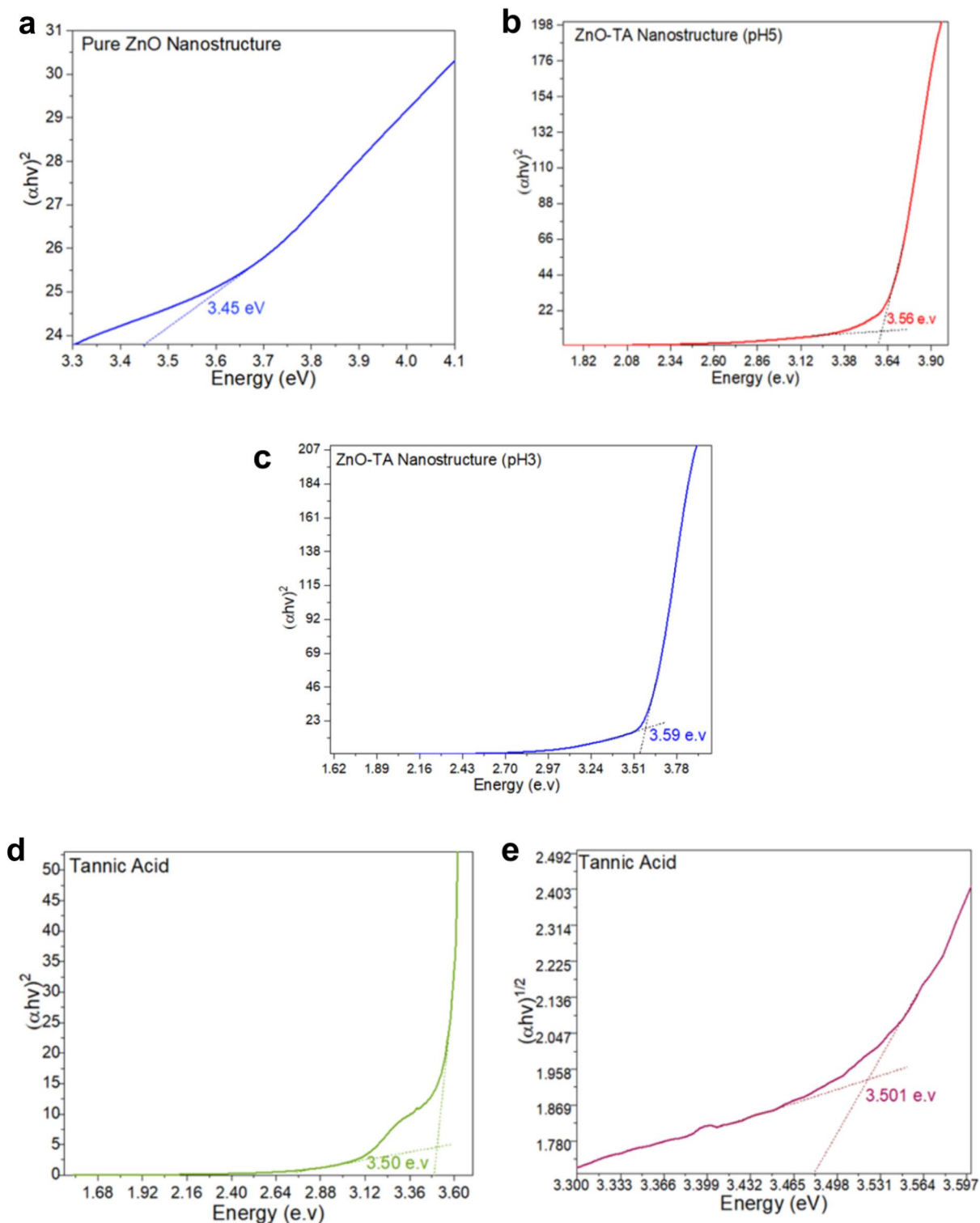


Figure 5. Optical absorption properties of the direct bandgap from the Tauc plot for (a) pure ZnO, (b) ZnO-TA pH 5, (c) ZnO-TA at pH 3 nanostructure. Tauc plot of (d) direct and (e) indirect bandgap TA structures.

Luminescence description

The emission spectrum of PL of pure ZnO nanostructures and the interaction condition between TA and ZnO nanostructures are presented in Fig. 7. The emission spectra for both pure ZnO and ZnO-TA nanostructures are normalised to confirm that the intensity of the NBE emission (zoom image) for the pure ZnO nanostructure sample is similar to that for the ZnO-TA nanostructures, as shown in Fig. 7a. The emitted emission intensity obtained at ~ 366 , ~ 365 and ~ 316 nm indicates the near band-edge emission (NBE) characteristic for pure ZnO and Zn-TA nanostructures, which arises from the recombination of the electrons in the valence band of the

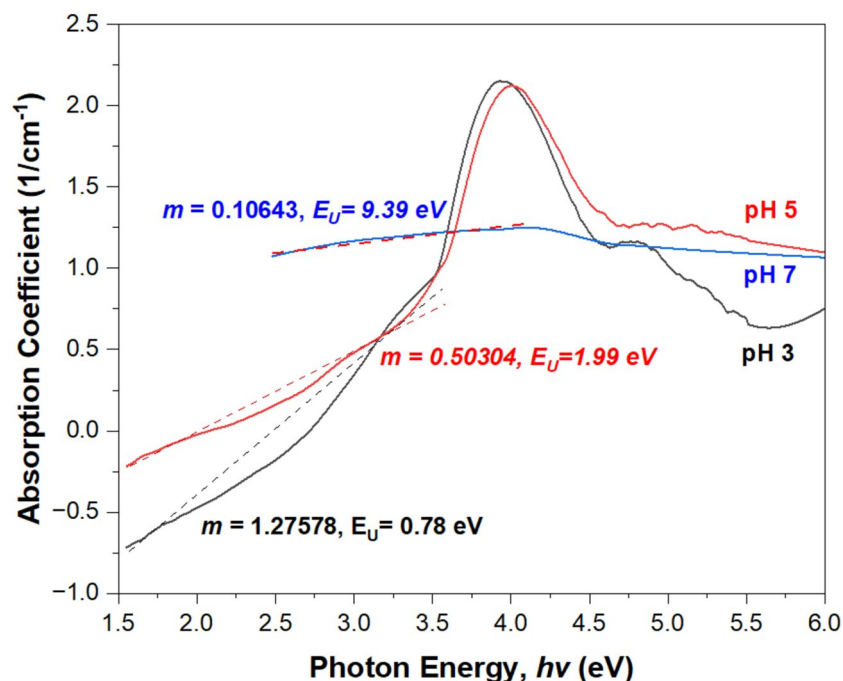


Figure 6. Dispersion of absorption coefficient, α in both pure ZnO and ZnO-TA nanostructures with the straight dash lines correspond to the approximation of the slope, m of each sample as a function of photon energy.

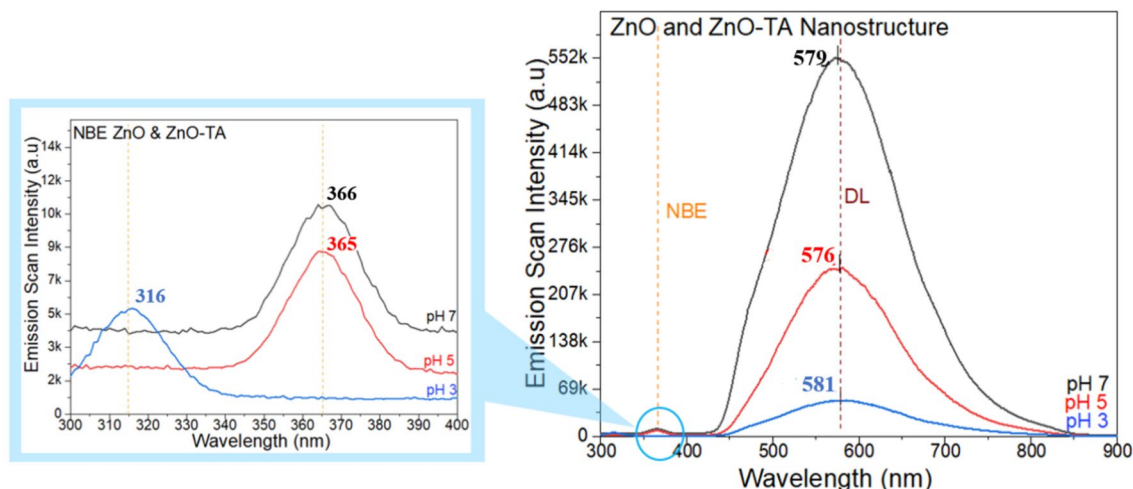
Sample	E_g (eV)	E_U (eV)
Pure ZnO (pH 7)	3.45	9.39
ZnO-TA (pH 5)	3.56	1.99
ZnO-TA (pH 3)	3.59	0.78

Table 2. The optical band gap, E_g and Urbach energy E_U of the corresponding samples.

ZnO. The wavelength of pure ZnO (pH 7) and ZnO-TA (pH 5) are not significantly shifted, while that ZnO-TA (pH 3) is clearly blue-shifted. Whilst the prominent, broad emission peak at longer wavelength in the range of ~ 576 to ~ 581 nm arises from the recombination effect of photo-excited holes in its conduction band with singly ionised Zn + O deficiencies, Zn interstitials and O antisites, causing deep-level (DL) trap emission⁷⁰. However, the O deficiencies are primarily responsible for the DL emission. It shall be noted that the emission intensity in the visible spectrum region (phosphorescence band range) for these samples is relatively discernible because of the significant structural defects. It is noted that the relative DL intensity ratio of the pH 7: pH 5: pH 3 samples is 11:5:1 and that the corresponding NBE intensity ratio is 4:3:2, demonstrating a decrease in the DL and NBE emission. Besides, the intensity ratio of DL to NBE of each sample is calculated where pure ZnO nanostructure (pH 7) shows a ratio of 52:1, which is higher compared to the ratio of ZnO-TA nanostructure with.

29:1 and 10:1 for samples of pH 5 and pH 3. The DL intensity for the ZnO-TA nanostructures was suppressed due to the increase in the excited electrons transferred from the ZnO to the TA, which reacts as an electron acceptor. Theoretically, the NBE emission from pure ZnO nanostructures is correlated with the excitons bound to shallow donors, whilst the DL emission is caused by the oxygen vacancy-related defects in ZnO nanostructures. For instance, the singly-ionised (Zn + O) oxygen vacancies create the recombination centres. The significant enhancement of the NBE emission from the ZnO-TA nanostructures formed due to the ZnO sheathing is indicated by the combination of the few identified effects. This reveals that the electrons from the phenolic hydroxyl of TA migrate mostly to the defect levels of the Zn atom. The TA outer layer augmented the carrier transfer between the ZnO core and the TA outer layer. Theoretically, as the ZnO core nanostructures are excited due to the interaction of the electron-hole pair, the photoelectrons and photon holes through the interface between the ZnO core and TA are generated. Upon the electron-hole recombination occurrence in both the ZnO core nanostructure and the TA outer layer take place, the photons are generated. The total amount of recombination probability is remarkably higher, and thus, the production of more photons is expected in the TA outer layer than in the ZnO core nanostructure. Hence, the ZnO core nanostructure emission is less intense than the TA layer. The last effect is the visible emission and non-radiative recombination (the cause of lowering the light generation efficiency and increasing heat losses) is squashed down, which causes a formation of depletion region at the

a



b

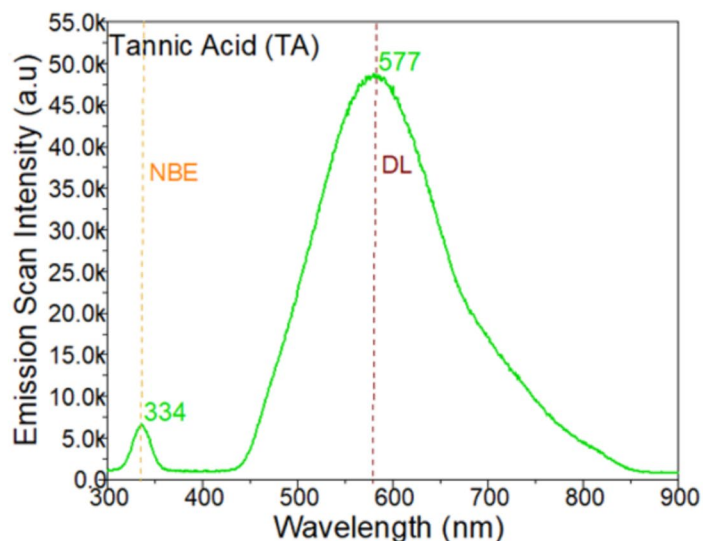


Figure 7. Normalised room temperature PL emission spectra by the defect emission band on (a) emission intensity of pure ZnO (pH 7) and ZnO-TA (pH 5 and pH 3) nanostructures and (b) wavelength of emission intensity of pure TA.

outer surface of the ZnO core nanostructure. This condition yields a condition where the Fermi energy level is reduced than the E_g levels at the defects related to visible emission (Zn interstitials and their complexes with O vacancies) and the non-radiative transition-related defects.

Structural analysis

The structural nature of the synthesised ZnO and ZnO-TA nanostructures is confirmed using XRD diffractogram as shown in Fig. 8. It is revealed that the polycrystalline wurtzite structure of ZnO with the observed peak positions in agreement with reported data in Joint Committee on Powder Diffraction Standards (JCPDS, card no: 043-0002 obtained from library) are indexed for hexagonal ZnO as indicated for pure ZnO (pH 7) and slightly added ZnO-TA sample (pH 5). Three prominent peaks are observed corresponding to the reflections from (100), (002) and (101) atomic planes of the ZnO phase. It shows the stability and the probable directions for grain growth which is considered as the minimum energy growth phase of ZnO crystal. The presence of other low-intensity reflections was demonstrated at (001), (102), (110), (103), (112) and (201) atomic planes of the hexagonal ZnO lattice. In all the test samples for pure ZnO nanostructures, no peak corresponding to other phases or elements emerged in the XRD analysis.

Further increase of TA concentration at pH 5 demonstrates the presence of similar typical ZnO atomic planes but with a reduction in intensity. This might be due to the dominance of TA molecular structure surrounding the

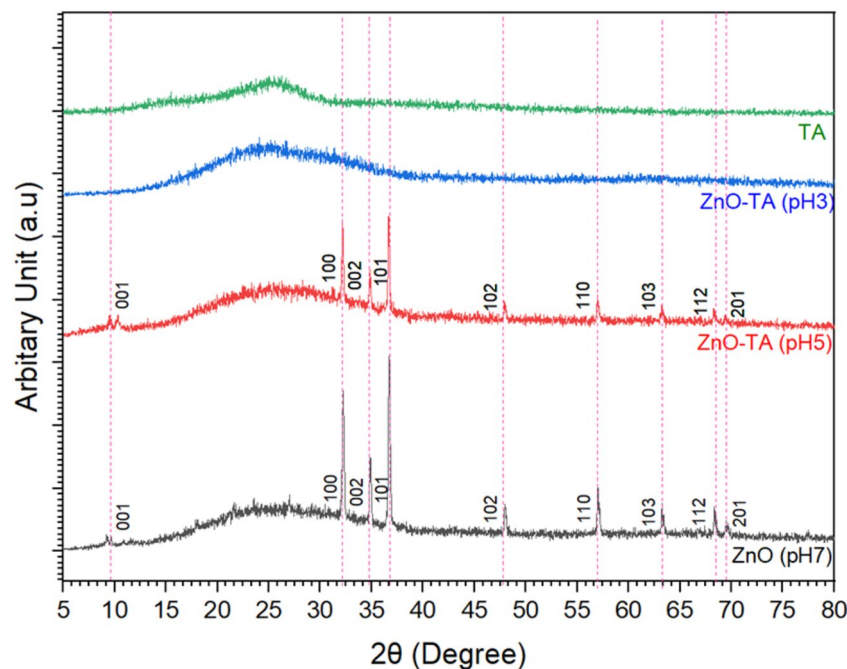


Figure 8. Powdered XRD diffractograms for pure ZnO (pH 7) and ZnO-TA prepared at pH 5 and pH 3 synthesised at 70 °C. The spectrum of TA is provided for comparison.

ZnO nanostructures as evinced by the aggregation condition indicated in the FESEM micrograph beforehand (Fig. 2b). Surprisingly, the highest added TA concentration in as-synthesised ZnO-TA nanostructures samples at pH 3 inhibits the dominance of the crystalline phase of ZnO indicated by vanishing the peak intensities. The dispel of the diffraction peaks positions of the ZnO nanostructures for the sample made at pH 3 implied the absence of any significant lattice on the ZnO wurtzite structure. Only TA molecules with amorphous spectrum structure in nature are exhibited as they imprinted over ZnO nanostructures in accordance with FESEM analysis.

The structural information on the crystallite size D , lattice parameters of α , c and V with position parameters u and ZnO bond length L for both pure ZnO and ZnO-TA nanostructures data obtained from the XRD results are tabulated in Table 3. The calculated D for pH 7 and pH 5 is 8.03 and 14.99 nm corresponding to pure ZnO and ZnO-TA nanostructures synthesised at 70 °C, respectively. The D of the pristine pure ZnO nanostructures is parallel to the particle size obtained from TEM which shows a significant decrease from 8 to 18 nm as the pure ZnO capped with TA molecule where the dominance of TA is indicated by the decrement of the crystal plane intensity. The obtained crystalline size shows a minor variation with the synthetic conditions. The pH 3 sample is completely amorphous and no crystallite size can be measured. It shall be noted that the percentage of Zn²⁺ release from the ZnO-TA nanostructures was contributed by the increase of TA concentration (decrease in pH). These results indicated that the TA caused the dissolution of ZnO nanostructures due to the modification effects of combined pH solution and complexation reaction.

The % crystallinity of the pure ZnO at pH 7 and ZnO-TA at pH 3 is compared. Only these two samples are valid since pH 3 is considered fully amorphous with the absence of ZnO peak. The % crystallinity indicated that pH 7 for pure ZnO nanostructures has approximately 43.75% crystallinity which is below 50%, having a semi-crystalline structure. This might be due to the variations in the synthesis parameters especially the

Pristine nanostructure	pH	D (nm)	Lattice parameters					Crystallinity (%)
			α (Å)	c (Å)	V (Å ³)	u	L (Å)	
ZnO	7	8.03	3.59	5.48	57.01	0.14	2.79	~43.75
ZnO-TA	5	14.99	2.63	5.49	57.12	0.07	3.06	~25.16
	3	Amorphous						
TA		Amorphous						

Table 3. The lattice parameters and the density of pristine ZnO (pH 7), and ZnO-TA (pH 5 and pH 3) evaluated from the XRD patterns. D is the crystalline diameter calculated from Debye–Scherrer's equation. The lattice parameters include the lattice constant α and c represent basal and height parameters, respectively, with the length L , volume V , and u representing internal atomic position.

ones synthesised through the sol–gel method. The pH 3 shows quite low crystallinity with value is approximately 25.16% which is confirmed by the weak diffraction spectrum corresponding to the elements discussed beforehand.

Antimicrobial against *S. aureus*

The pure ZnO (pH 7) and ZnO-TA (pH 3) nanostructure samples are tested against *S. aureus* microbe at ambient temperature (35 °C). The antibacterial activities of pure ZnO and ZnO-TA nanostructures are assayed based on the concentration of the bacteria recovered from the inoculated treated test. The results demonstrated that the suspended bacteria remained mostly viable over 5 min. In contrast, the survival rates of *S. aureus* exposed to pure ZnO and ZnO-TA nanostructures declined to 99.39% and 99.69% within 24 h. The observation is mainly attempted to quantify according to the bacterial survival rate based on the loss in microbial viability with time. The details of the test carried out for both samples are summarised in Table 4. Both samples showed positive performance in inhibiting the growth of the *S. aureus* microbe.

Figure 9 shows the pictures of *S. aureus* microbe exposed to pure ZnO and ZnO-TA nanostructures for 24 h in Fig. 9a,b, respectively. The cloudy brown colour shows the spot of *S. aureus* growth. These results indicated that the antibacterial efficacy of ZnO-TA nanostructures was slightly higher than that of pure ZnO nanostructures. This can be ascribed to the benefits of TA-capped ligands and the slight limitation of ZnO nanostructures⁵¹. ZnO-TA nanostructure sample had a d_m of 18 ± 0.4 nm that eased the attachment to the surface of the organism and the positive surface charge on ZnO-TA nanostructures enables a straightforward inter-particle interaction and the negatively charged organism membranes. Additionally, *S. aureus*, a strain organism representing Gram-positive bacteria, displayed a delicate survival rate compared to other famous organism strains, such as *E. coli*. Hence, it reduces the resistant efficiency towards the antibacterial effect of the ZnO-TA nanostructures. These results support the previous assumption that *S. aureus* could not tolerate the ZnO-TA nanostructure medium.

It is also found that the pH of the nanostructure medium influences the amount of survival bacteria strain. It is shown that lowering the pH value enabled the quick and effective killing of up to 99.69% of *S. aureus* strain within 24 h. The explanations are based on these three reasons. First, the non-existence of the outer membrane layer and the existence of teichoic acid molecules of negatively charged bacteria within a thick peptidoglycan cell wall (20–80 nm) on the surface of *S. aureus* induced higher attraction towards the positively charged. It yielded a more specific site to be disrupted by positively charged molecules. Second, the *S. aureus* owns a minimal number of tiny channels of porins within the outer membrane that are used to block the access of the particles into the strain cell, making them defenceless. The last one, *S. aureus*, has a small dimension (sphere, internal diameter, ~0.5 to 1 μ m) that may account for more detailed interaction with the ZnO-TA nanoparticles, resulting in better antibacterial activity compared to the larger size bacteria strain. Capping TA with ZnO nanostructure also results in aggregation, and this nanoparticle aggregation influences macrophage cytotoxicity. As the nanostructures aggregated, they were found to secrete more cytotoxin, degrading the cytoplasm of the microbe and inhibiting its growth.

Conclusion

Pure ZnO (pH 7) and ZnO-TA (pH 5 and pH 3) nanostructures are successfully synthesised with ZnO-TA samples, showing favour of aggregation as a higher concentration of TA is introduced to the nanostructure. The study reveals that the bonding description is monopolised by the TA in ZnO-TA nanostructure with significant stretching representing C=O (carboxylate) and slightly C–H bond (aromatic ester), which are associated with the phenolic group of TA. The outcome of the optical absorption analysis shows that the TA influenced the wider E_g of the ZnO-TA nanostructure from the interaction of the unshared electrons of oxygen in the isolated phenyl group of TA. The Urbach energy increased with the decrease of E_g with a low value obtained at pH 3 indicating a low structural system as evinced further by the crystallinity results. The reported results of PL emission demonstrated that the ratio of DL to NBE for ZnO-TA samples is slightly smaller than the pure ZnO nanostructure. The truncation of the ratio is caused by the increase in the excited electrons transferred from the ZnO to the TA, which reacts as an electron acceptor. The crystallinity difference originated from the influence of TA concentration that yields different pH values. Higher TA concentration reduced the crystal quality of ZnO nanostructures and at pH 3, the sample became totally amorphous without any ZnO peaks. Also, with the addition of TA, the efficiency inhibits the growth of *S. aureus* is slightly improved as the acidic condition and the ester bond of TA influenced the destruction of the microbe's cell membrane. Thus, adding a higher concentration of TA shows

Nanostructure sample	Bacteria concentration 5 min after inoculation (CPU/sample)	Bacteria concentration 24 h after inoculation (CPU/sample)	Per cent of bacterial reduction after 24 h (%)
Pure ZnO	1.02×10^5	6.22×10^2	99.39
ZnO-TA	1.02×10^5	3.08×10^2	99.69
Controlled sample (<i>S. aureus</i> without treatment)	1.02×10^5	$> 1.02 \times 10^5$	Null

Table 4. AATCC 100 assessment result of microbes inhibitory between pure ZnO (pH 7) and ZnO-TA (pH 3) nanostructure against *S. aureus* species. Notice that the performance of ZnO-TA nanostructure against microbes *S. aureus* is slightly better than pure ZnO nanostructure due to the presence of the phenolic compound and acidic condition. A bacterial colony counter machine counts bacterial concentration.

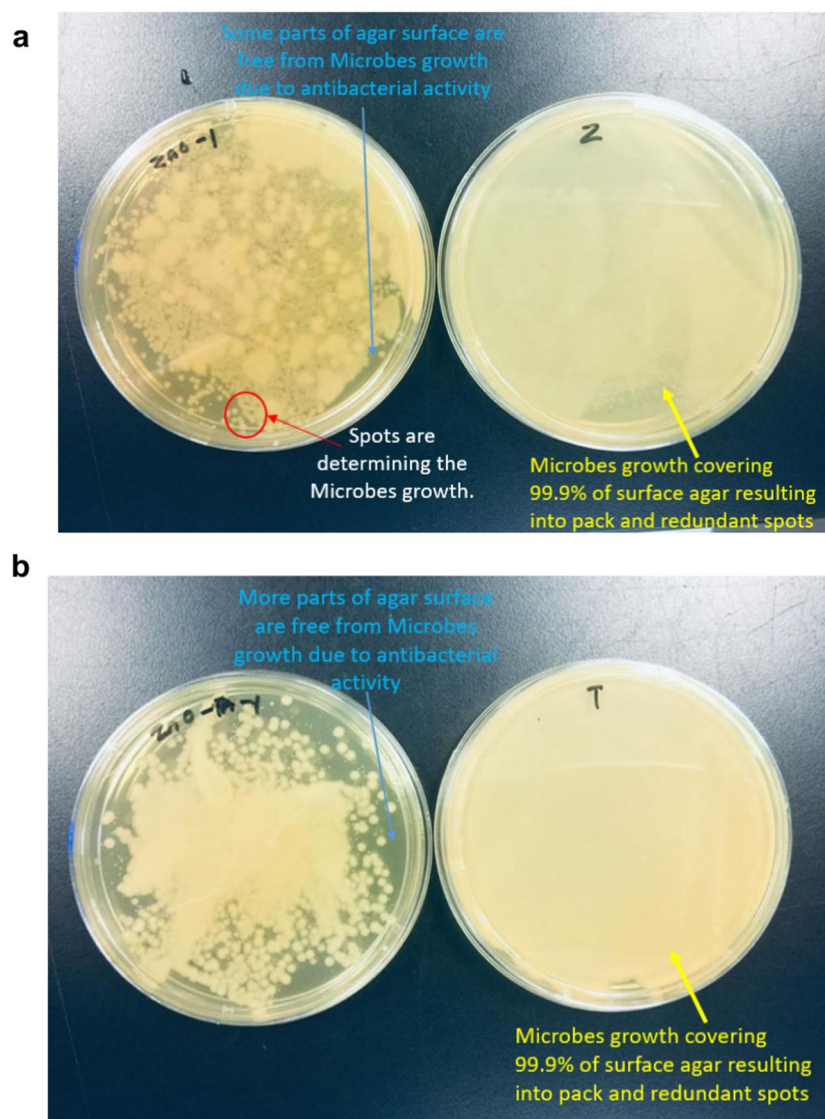


Figure 9. Total viable microbes count for (a) pure ZnO nanostructure and (b) ZnO-TA nanostructure 24 h after inoculation. Z and T represent the control (*Staphylococcus aureus* without treatment).

slightly better performance in optical characteristics and the antimicrobial properties of ZnO nanostructure. The works hold significant importance in the field of ZnO nanostructures as surface function materials that possess efficient physicochemical and antibacterial properties.

Data availability

The datasets used and/or analysed during the current study available from the corresponding author on reasonable request.

Received: 22 January 2024; Accepted: 7 August 2024

Published online: 10 August 2024

References

- Khalifa, I., Zhu, W., Mohammed, H. H. H., Dutta, K. & Li, C. Tannins inhibit SARS-CoV-2 through binding with catalytic dyad residues of 3CLpro: An in silico approach with 19 structural different hydrolysable tannins. *J. Food Biochem.* **44**(10), e13432 (2020).
- Haapakoski, M. *et al.* Antiviral functionalization of cellulose using tannic acid and tannin-rich extracts. *Front. Microbiol.* **14**, 1287167 (2023).
- Wang, S.-C., Chou, I.-W. & Hung, M.-C. Natural tannins as anti-SARS-CoV-2 compounds. *Int. J. Biol. Sci.* **18**(12), 4669 (2022).
- Jing, W., Xiaolan, C., Yu, C., Feng, Q. & Haifeng, Y. Pharmacological effects and mechanisms of tannic acid. *Biomed. Pharmacother.* **154**, 113561 (2022).
- Wang, S.-C. *et al.* Tannic acid suppresses SARS-CoV-2 as a dual inhibitor of the viral main protease and the cellular TMPRSS2 protease. *Am. J. Cancer Res.* **10**(12), 4538 (2020).

6. Chen, C.-Y. *et al.* Tannic acids and proanthocyanidins in tea inhibit SARS-CoV-2 variants infection. *Am. J. Cancer Res.* **14**(5), 2555 (2024).
7. Jindal, D. & Rani, V. In silico studies of phytoconstituents from Piper longum and Ocimum sanctum as ACE2 and TMRSS2 inhibitors: Strategies to combat COVID-19. *Appl. Biochem. Biotechnol.* **195**(4), 2618–2635 (2023).
8. Yang, G. *et al.* Noncovalent co-assembly of aminoglycoside antibiotics@ tannic acid nanoparticles for off-the-shelf treatment of pulmonary and cutaneous infections. *Chem. Eng. J.* **474**, 145703 (2023).
9. Wang, H. *et al.* Tannin coordinated nanozyme composite-based hybrid hydrogel eye drops for prophylactic treatment of multidrug-resistant *Pseudomonas aeruginosa* keratitis. *J. Nanobiotechnol.* **20**(1), 445 (2022).
10. Tian, S. *et al.* Green synthesis of silver nanoparticles using sodium alginate and tannic acid: Characterization and anti *S. aureus* activity. *Int. J. Biol. Macromol.* **195**, 515–522 (2022).
11. Heidari, F., Akbarzadeh, I., Nourouzian, D., Mirzaie, A. & Bakhshandeh, H. Optimization and characterization of tannic acid loaded niosomes for enhanced antibacterial and anti-biofilm activities. *Adv. Powder Technol.* **31**(12), 4768–4781 (2020).
12. He, X. *et al.* Tannic acid-reinforced methacrylated chitosan/methacrylated silk fibroin hydrogels with multifunctionality for accelerating wound healing. *Carbohydr. Polym.* **247**, 116689 (2020).
13. dos Santos, J. F. *et al.* Indirect inhibitory activity of pyrogallol against the Tet (K) efflux pump by a membrane effect: In vitro and in silico approach. *Process Biochem.* **107**, 138–144 (2021).
14. Nassarawa, S. S. *et al.* Chemical aspects of polyphenol-protein interactions and their antibacterial activity. *Crit. Rev. Food Sci. Nutr.* **63**(28), 9482–9505 (2023).
15. Chetri, S. The culmination of multidrug-resistant efflux pumps vs. meager antibiotic arsenal era: Urgent need for an improved new generation of EPIs. *Front. Microbiol.* **14**, 1149418 (2023).
16. Zack, K. M., Sorenson, T. & Joshi, S. G. Types and mechanisms of efflux pump systems and the potential of efflux pump inhibitors in the restoration of antimicrobial susceptibility, with a special reference to acinetobacter baumannii. *Pathogens* **13**(3), 197 (2024).
17. Zhou, H., Dai, R., Wang, T. & Wang, Z. Enhancing stability of tannic acid-FeIII nanofiltration membrane for water treatment: Intercoordination by metal-organic framework. *Environ. Sci. Technol.* **56**(23), 17266–17277 (2022).
18. Dong, J. *et al.* Facile, smart, and degradable metal-organic framework nanopesticides gated with FeIII-tannic acid networks in response to seven biological and environmental stimuli. *ACS Appl. Mater. Interfaces* **13**(16), 19507–19520 (2021).
19. Kim, N., Lee, I., Choi, Y. & Ryu, J. Molecular design of heterogeneous electrocatalysts using tannic acid-derived metal-phenolic networks. *Nanoscale* **13**(48), 20374–20386 (2021).
20. Chang, T.-W. *et al.* Tannic acid-induced interfacial ligand-to-metal charge transfer and the phase transformation of Fe₃O₄ nanoparticles for the photothermal bacteria destruction. *Chem. Eng. J.* **428**, 131237 (2022).
21. Zhang, L., Guan, Q., Jiang, J. & Khan, M. S. Tannin complexation with metal ions and its implication on human health, environment and industry: An overview. *Int. J. Biol. Macromol.* **253**, 127485 (2023).
22. Abebe, B., Zereffa, E. A., Tadesse, A. & Murthy, H. A. A review on enhancing the antibacterial activity of ZnO: Mechanisms and microscopic investigation. *Nanoscale Res. Lett.* **15**, 1–19 (2020).
23. Gudkov, S. V. *et al.* A mini review of antibacterial properties of ZnO nanoparticles. *Front. Phys.* **9**, 641481 (2021).
24. Mendes, C. R. *et al.* Antibacterial action and target mechanisms of zinc oxide nanoparticles against bacterial pathogens. *Sci. Rep.* **12**(1), 2658 (2022).
25. Zhu, X. *et al.* Dissection of the antibacterial mechanism of zinc oxide nanoparticles with manipulable nanoscale morphologies. *J. Hazard. Mater.* **430**, 128436 (2022).
26. Barma, M. D., Muthupandiyam, I., Samuel, S. R. & Amaechi, B. T. Inhibition of Streptococcus mutans, antioxidant property and cytotoxicity of novel nano-zinc oxide varnish. *Archiv. Oral Biol.* **126**, 105132 (2021).
27. Ramesh, A. M. *et al.* Antioxidant and photocatalytic properties of zinc oxide nanoparticles phyto-fabricated using the aqueous leaf extract of Sida acuta. *Green Process. Synth.* **11**(1), 857–867 (2022).
28. Singh, T. A. *et al.* A state of the art review on the synthesis, antibacterial, antioxidant, antidiabetic and tissue regeneration activities of zinc oxide nanoparticles. *Adv. Coll. Interface Sci.* **295**, 102495 (2021).
29. Farazin, A., Mohammadimehr, M. & Naeimi, H. Flexible self-healing nanocomposite based gelatin/tannic acid/acrylic acid reinforced with zinc oxide nanoparticles and hollow silver nanoparticles based on porous silica for rapid wound healing. *Int. J. Biol. Macromol.* **241**, 124572 (2023).
30. Yang, C. M., Lee, J., Lee, H. & Park, W. H. ZnO nanoparticle-embedded modified silk fibroin-tannin multifunctional hydrogel. *Int. J. Biol. Macromol.* **210**, 1–10 (2022).
31. Yang, C. M. *et al.* Silk fibroin/tannin/ZnO nanocomposite hydrogel with hemostatic activities. *Gels* **8**(10), 650 (2022).
32. Panchal, P. *et al.* Biogenic mediated Ag/ZnO nanocomposites for photocatalytic and antibacterial activities towards disinfection of water. *J. Coll. Interface Sci.* **563**, 370–380 (2020).
33. He, G., Wan, M., Wang, Z., Zhao, Y. & Sun, L. Fabrication of firm, superhydrophobic and antimicrobial PVDF@ ZnO@ TA@ DT electrospun nanofibrous membranes for emulsion separation. *Coll. Surf. A Physicochem. Eng. Aspects* **662**, 130962 (2023).
34. Jafari, H. *et al.* Tannic acid: A versatile polyphenol for design of biomedical hydrogels. *J. Mater. Chem. B* **10**(31), 5873–5912 (2022).
35. Chen, C., Yang, H., Yang, X. & Ma, Q. Tannic acid: A crosslinker leading to versatile functional polymeric networks: A review. *RSC Adv.* **12**(13), 7689–7711 (2022).
36. Vong, C. I., Rathinasabapathy, T., Moncada, M. & Komarnitsky, S. All polyphenols are not created equal: Exploring the diversity of phenolic metabolites. *J. Agric. Food Chem.* **70**(7), 2077–2091 (2022).
37. Yin, Y., Zhang, Y., Xie, Q., He, Y. & Guo, J. Controlled self-assembly of natural polyphenols driven by multiple molecular interactions. *ChemPlusChem* **89**(5), e202300695 (2024).
38. Dong, Y. *et al.* A facile one-step self-assembly strategy for constructing biocompatible and pH-sensitive polyphenol-based nanoparticles for high-efficiency tumor therapy. *J. Ind. Eng. Chem.* **136**, 420–429. <https://doi.org/10.1016/j.jiec.2024.02.031> (2024).
39. Wang, X., Fan, Y., Yan, J. & Yang, M. Engineering polyphenol-based polymeric nanoparticles for drug delivery and bioimaging. *Chem. Eng. J.* **439**, 135661 (2022).
40. Raviolo, A., Farré, A. S. & Schroh, N. T. Students' understanding of molar concentration. *Chem. Educ. Res. Practice* **22**(2), 486–497 (2021).
41. Klein, J. *et al.* Limitations of the Tauc plot method. *Adv. Funct. Mater.* **33**(47), 2304523 (2023).
42. Zhong, H. *et al.* Idealizing Tauc plot for accurate bandgap determination of semiconductor with ultraviolet-visible spectroscopy: A case study for cubic boron arsenide. *J. Phys. Chem. Lett.* **14**(29), 6702–6708 (2023).
43. Archana, K. J., Preetha, A. C. & Balasubramanian, K. Influence of Urbach energy in enhanced photocatalytic activity of Cu doped ZnO nanoparticles. *Opt. Mater.* **127**, 112245 (2022).
44. Haris, M. P., Kazim, S. & Ahmad, S. Microstrain and Urbach energy relaxation in FAPbI₃-based solar cells through powder engineering and perfluoroalkyl phosphate ionic liquid additives. *ACS Appl. Mater. Interfaces* **14**(21), 24546–24556 (2022).
45. Ugur, E. *et al.* Life on the Urbach edge. *J. Phys. Chem. Lett.* **13**(33), 7702–7711 (2022).
46. Basak, M., Rahman, M. L., Ahmed, M. F., Biswas, B. & Sharmin, N. The use of X-ray diffraction peak profile analysis to determine the structural parameters of cobalt ferrite nanoparticles using Debye-Scherrer, Williamson-Hall, Halder-Wagner and Size-strain plot: Different precipitating agent approach. *J. Alloys Compd.* **895**, 162694 (2022).
47. Garg, A., Parmar, L. K., Dager, H. S., Bhardwaj, P. & Yadav, A. Structural and dielectric analysis of Cu-doped NiCo₂O₄ nanoparticles synthesized by green synthesis approach. *Chem. Phys. Impact* **8**, 100639 (2024).

48. Vydrina, I. *et al.* A new method for determination of lignocellulose crystallinity from XRD data using NMR calibration. *Carbohydrate Polym. Technol. Appl.* **5**, 100305 (2023).
49. Jadhav, D. A. & Ghangrekar, M. M. Optimising the proportion of pure and mixed culture in inoculum to enhance the performance of microbial fuel cells. *Int. J. Environ. Technol. Manag.* **23**(1), 50–67 (2020).
50. Liu, L. *et al.* Connecting energetics to dynamics in particle growth by oriented attachment using real-time observations. *Nat. Commun.* **11**(1), 1045 (2020).
51. Jun, Y.-S. *et al.* Classical and nonclassical nucleation and growth mechanisms for nanoparticle formation. *Annu. Rev. Phys. Chem.* **73**, 453–477 (2022).
52. Jebur, S. M. & Kareem, J. A. The leaching behavior of zinc oxide in medical waste of dental clinics. *J. Eng.* **29**(5), 146–155 (2023).
53. Ranjbari, A., Demeestere, K., Kim, K.-H. & Heynderickx, P. M. Oxygen vacancy modification of commercial ZnO by hydrogen reduction for the removal of thiabendazole: Characterization and kinetic study. *Appl. Catal. B Environ.* **324**, 122265 (2023).
54. Zeinalipour-Yazdi, C. D. & Loizidou, E. Z. An experimental FTIR-ATR and computational study of H-bonding in ethanol/water mixtures. *Chem. Phys.* **550**, 111295 (2021).
55. Nejad, A., Li, X., Zhu, T., Liu, Y. & Duan, C. Mid-infrared laser spectroscopy of jet-cooled formic acid trimer: Mode-dependent line broadening in the C–O stretching region. *J. Phys. Chem. Lett.* **14**(35), 7795–7801 (2023).
56. Salim, R. M., Asik, J. & Sarjadi, M. S. Chemical functional groups of extractives, cellulose and lignin extracted from native *Leucaena leucocephala* bark. *Wood Sci. Technol.* **55**(2), 295–313. <https://doi.org/10.1007/s00226-020-01258-2> (2021).
57. de Almeida, W. L., Rodembusch, F. S., Ferreira, N. S. & de Sousa, V. C. Eco-friendly and cost-effective synthesis of ZnO nanoparticles by Tapioca-assisted sol-gel route. *Ceram. Int.* **46**(8), 10835–10842 (2020).
58. Karimian, A., Namvar-Mahboub, M., Binabaji, F. & Rajabi, S. Tannic Acid-Cu-modified Fe₃O₄@ SiO₂ nanoparticles (Fe₃O₄@ SiO₂@ TA-Cu NPs): New recyclable magnetic catalyst for the three-component synthesis of 2-amino-3, 5-dicarbonitrile-6-thio-pyridines. *J. Iran. Chem. Soc.* **19**(11), 4397–4409 (2022).
59. Firdous, S. O., Arif, K., Wong, S. Y., Li, X. & Arafat, M. T. In situ crosslinked electrospun gelatin matrix with unoxidized tannic acid through stable hydrogen bonding. *J. Appl. Polym. Sci.* **140**(43), e54572 (2023).
60. Wang, T.-X., Ding, X. & Han, B.-H. Tannic acid-based hypercrosslinked polymer as heterogeneous catalyst for aerobic oxidation reaction. *Polymer* **259**, 125344 (2022).
61. Zhang, Z., Li, S., Liu, X., Bian, H. & Huang, G. In-situ synthesis of zinc oxide-tannic acid-waste bagasse with antibacterial activity as multifunctional additive for packaging film. *J. Clean. Prod.* **467**, 142934 (2024).
62. Espina, A., Cañamares, M. V., Jurasekova, Z. & Sanchez-Cortes, S. Analysis of iron complexes of tannic acid and other related polyphenols as revealed by spectroscopic techniques: Implications in the identification and characterization of iron gall inks in historical manuscripts. *ACS Omega* **7**(32), 27937–27949 (2022).
63. Gharpure, S., Yadwade, R. & Ankamwar, B. Non-antimicrobial and non-anticancer properties of ZnO nanoparticles biosynthesized using different plant parts of *Bixa orellana*. *ACS Omega* **7**(2), 1914–1933 (2022).
64. Dong, Y., Zhang, D., Li, D., Jia, H. & Qin, W. Control of Ostwald ripening. *Sci. China Mater.* **66**(3), 1249–1255 (2023).
65. Leffler, V., Ehlert, S., Forster, B., Dulle, M. & Förster, S. Nanoparticle heat-up synthesis: In situ X-ray diffraction and extension from classical to nonclassical nucleation and growth theory. *ACS Nano* **15**(1), 840–856 (2021).
66. Li, Y., Cheng, G., Zhang, M., Cao, Y. & Von Lau, E. Advances in depressants used for pyrite flotation separation from coal/minerals. *Int. J. Coal Sci. Technol.* **9**(1), 54 (2022).
67. Yin, B. *et al.* Superatomic signature and reactivity of silver clusters with oxygen: Double magic Ag₁₇—with geometric and electronic shell closure. *CCS Chem.* **3**(12), 219–229 (2021).
68. Weber, F., Sagstuen, E., Zhong, Q.-Z., Zheng, T. & Tiainen, H. Tannic acid radicals in the presence of alkali metal salts and their impact on the formation of silicate-phenolic networks. *ACS Appl. Mater. Interfaces* **12**(47), 52457–52466 (2020).
69. Saikukulov, F., Sapaev, B., Nasimov, K., Kurbanova, D. & Tursunova, N. Structure, aromatic properties and preparation of the quinazolin-4-one molecule. *E3S Web Conf.* **389**, 03075. <https://doi.org/10.1051/e3sconf/202338903075> (2023).
70. Kumar, M. & Dhar, J. C. Defect engineering of RF sputtered Mg doped ZnO thin film for efficient photodetector application. *Micro Nanostruct.* **185**, 207724 (2024).

Acknowledgements

Universiti Malaysia Pahang Al-Sultan Abdullah (UMPSA) fully supports the facilities and resources for this research. The authors would like to acknowledge the support of the internal grants of Universiti Malaysia Pahang Al-Sultan Abdullah (RDU2203105).

Author contributions

Conceptualisation, N.A.C.L.; methodology, N.A.C.L.; software, N.A.C.L.; validation, N.A.C.L. and A.K.; formal analysis, N.A.C.L. and A.K.; investigation, N.A.C.L. and A.K.; resources, N.A.C.L.; data curation, N.A.C.L. and A.K.; writing—original draft preparation, N.A.C.L. and A.K.; writing—review and editing, N.A.C.L. and A.K.; visualisation, N.A.C.L.; supervision, N.A.C.L.; project administration, N.A.C.L.; funding acquisition, N.A.C.L. All authors have read and agreed to the published version of the manuscript.

Funding

The research work is entirely funded by the internal grants of Universiti Malaysia Pahang Al-Sultan Abdullah (RDU2203105).

Competing interests

The authors declare no competing interests.

Additional information

Correspondence and requests for materials should be addressed to N.A.C.L.

Reprints and permissions information is available at www.nature.com/reprints.

Publisher's note Springer Nature remains neutral with regard to jurisdictional claims in published maps and institutional affiliations.

Open Access This article is licensed under a Creative Commons Attribution-NonCommercial-NoDerivatives 4.0 International License, which permits any non-commercial use, sharing, distribution and reproduction in any medium or format, as long as you give appropriate credit to the original author(s) and the source, provide a link to the Creative Commons licence, and indicate if you modified the licensed material. You do not have permission under this licence to share adapted material derived from this article or parts of it. The images or other third party material in this article are included in the article's Creative Commons licence, unless indicated otherwise in a credit line to the material. If material is not included in the article's Creative Commons licence and your intended use is not permitted by statutory regulation or exceeds the permitted use, you will need to obtain permission directly from the copyright holder. To view a copy of this licence, visit <http://creativecommons.org/licenses/by-nc-nd/4.0/>.

© The Author(s) 2024